Nano Research

Open Access

Research Article

Blocked bioorthogonal chemistry enabled switchable bioorthosome to improve liposomal drug delivery for glioblastoma therapy

Chao Wang[1,2], Jie Wu[2], Zhiran Duan[2], Yuqing Pan[2], Haijing Qu[2], Wei Cheng[2], Ning Wang[2], Han Chen[2], Xiaoli Gao[1], Mengqing Hou[1], Ying Zhang[1] ✉, and Xiangdong Xue[2] ✉

[1] *Key Laboratory of Resource Biology and Biotechnology of Western China, Ministry of Education, Provincial Key Laboratory of Biotechnology, College of Life Sciences, Northwest University, Xi'an 710069, China*

[2] *Shanghai Frontiers Science Center of Drug Target Identification and Delivery, School of Pharmaceutical Sciences, National Key Laboratory of Innovative Immunotherapy, Shanghai Jiao Tong University, Shanghai 200240, China*

Cite this article: *Nano Research*, **2025**, *18*, 94907338. https://doi.org/10.26599/NR.2025.94907338

ABSTRACT: Glioblastoma (GBM) interventions necessitate exceptional precision due to the presence of blood-brain barrier (BBB) and its intricate co-growth with neuron and glial cells. Here, we developed a blocked bioorthogonal chemistry enabled liposome, termed Bioorthosome, with switchable BBB-crossing ligand that could block the bioorthogonal moieties in normal tissue and blood circulation. Upon traversing the BBB and reaching tumor region, the BBB-crossing ligand could detach from the Bioorthosome under acidic tumor microenvironment and switch to the bioorthogonal moieties to react with the metabolically expressed azide-containing sialylations on GBM cell surface. This switchable bioorthogonal chemistry ensures that only GBM cells are targeted, thereby enhancing the precision of liposomal drug delivery. *In vitro* and *in vivo* studies have demonstrated that the Bioorthosome efficiently crosses the BBB and undergoes a ligand-switching process to selectively recognize GBM cells while sparing normal brain tissue, leading to enhanced therapeutic efficacy and reduced off-target accumulation. By integrating bioorthogonal reactions with a tumor microenvironment-responsive ligand-switching mechanism, our Bioorthosome design overcomes the limitations of inefficient BBB permeability and suboptimal anti-GBM drug delivery, paving the way for more precise GBM-targeted therapies and the advancement of more effective treatment strategies.

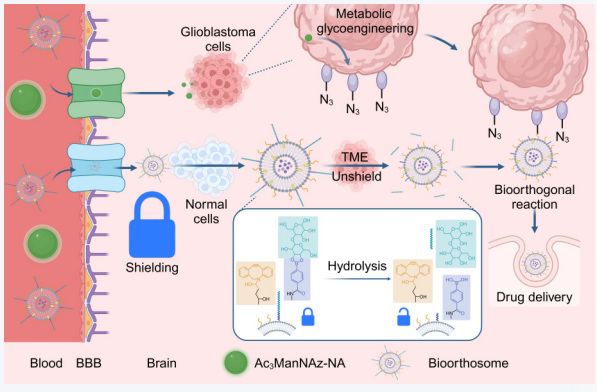

KEYWORDS: glioblastoma, bioorthogonal chemistry, blood–brain barrier, liposome, tumor-targeting

1 Introduction

Glioblastoma multiforme (GBM) is the leading cause of mortality in patients with primary brain tumor [1]. Despite chemotherapy being a standard treatment modality for GBM, the effectiveness of numerous anti-tumor agents is significantly hampered by the presence of the blood-brain barrier (BBB) and the blood-brain tumor barrier (BBTB) [2–4]. GBM is also characterized by its highly invasive nature, infiltrating surrounding normal brain tissue and disseminating along neural pathways and vascular structures. Therefore, a precision drug delivery strategy is necessary to prevent toxic drug accumulation in healthy brain tissue while strengthening its anti-tumor functionality in GBM treatment [5].

Nanomedicines have attracted substantial interests in biomedical research as multifunctional platforms, serving as vectors either for contrast or therapeutic agents to improve their tumor accumulation [6–9]. The passage of essential nutrients across the BBB is mediated by a variety of transporters, including glucose transporter 1 (GLUT1) [10–12], low-density lipoprotein receptor–related protein-1 (LRP-1) [13, 14], etc. Capitalizing on the high substrate specificity of these transport proteins, it is feasible to augment the delivery of pharmaceuticals to the brain by chemically modifying nanomedicines with the substrates that are recognized by these transporters [15–16]. Nonetheless, despite successful traversal of the BBB or BBTB via this strategy, the lack of tumor selectivity still poses a significant risk of detrimental effects on normal brain tissue [17–19].

Received: January 9, 2025; **Revised:** February 15, 2025
Accepted: February 26, 2025

✉Address correspondence to Ying Zhang, zhangying@nwu.edu.cn; Xiangdong Xue, xuexd@sjtu.edu.cn

To improve tumor specificity, active-targeting strategies involving the conjugation of biological moieties such as antibodies, aptamers, or peptides to the nanoparticle surface have demonstrated the potential to increase the selectively GBM targeting by ligand-receptor interactions [20–23]. However, the saturation of the receptors, coupled with the limited disease specificity, often restricts the capacity for ligand-receptor mediated targeting delivery and leads to off-target accumulation in healthy tissues, resulting in unintended drug release and adverse side effects [24]. Bioorthogonal chemistry has emerged as a promising avenue in the biomedical field, owing to its ability to facilitate highly specific and biocompatible chemical reactions in living systems. Metabolic glycoengineering allows the production of reactive groups containing glycoconjugates on the surface of target cells when treated with reactive groups containing glycoside [25]. This selective labeling mechanism pioneered by the Bertozzi group has applications in diverse areas such as polysaccharide analysis, three-dimensional cell assembly, and metabolic pathway elucidation [26–29]. Tumor cells, characterized by aberrant glycosylation and significant elevated levels of sialylation relative to healthy cells, offer a desirable possibility to enhance the dose-dependent expression of tumor-related glycan targets [30]. Hence, the combination of metabolic glycoengineering with bioorthogonal chemistry holds the promise of significantly improving the tumor-targeting capabilities of nanomedicines [31–33]. However, the metabolic approach may not preclude the possibility of bioorthogonal moieties being expressed on normal cells, as these cells can also uptake the exogenous glycosides, thereby risking the rather low delivery level of therapeutics to normal brain cells. Obviously, the tumor-targeting interventions of GBM still face challenges. Therefore, there is considerable room for advancement in the refinement of bioorthogonal targeting strategies, particularly in brain tumor treatments that need high precision.

The approach of attaching carbohydrate analogues to neuroactive molecules provides an efficient strategy for facilitating MGE molecules entry into the central nervous system by crossing the BBB [34]. In this study, we synthesized an azide-containing glycoside, Ac_3ManNAz-NA (AMN), a mannose derivative capable of crossing the BBB through niacin receptor HCAR2 and undergoing a metabolic glycoengineering process to introduce N-azidoacetyl-D-neuraminic acid (NeuAz)-containing sialylations (azides) on GBM cell surfaces, offering the potential for tumor-targeting intervention based on bioorthogonal click chemistry. To avoid the potential risk of bioorthogonal targeting to the azides on normal cells during the metabolic glycoengineering, we proposed a blocked bioorthogonal chemistry-enabled liposome, termed Bioorthosome, equipped with a switchable BBB-crossing ligand to shield bioorthogonal moieties on a liposome. To construct bioorthosome, dibenzocyclooctyne (DBCO) and phenylboronic acid (PBA) modified DSPE-PEG_{2000} are employed to construct a dual-functionalized liposome with both two moieties on the surface (Scheme 1(a)). Then, GLUT1 substrates (maltose, MA) [35] are introduced to the surface of the dual-functionalized liposome through an acid-cleavable boronic ester (PBA-MA) to create the final Bioorthosome. The MA ligand not only facilitates BBB crossing but also serves as shielding for DBCO moieties to prevent undesirable bioorthogonal reactions with azides that are also expressed on the normal cells. This design allows the Bioorthosome to remain inert in normal tissue and blood circulation, while becoming active within acidic tumor microenvironment (TME); the MA would be detached at acidic TME to remove shielding and enable bioorthogonal chemistry-mediated targeting to azide tags on GBM cells (Scheme 1(b)), thus leading to a high tumor specificity of our Bioorthosome. In an intracranial glioblastoma mouse model, our Bioorthosome efficiently crosses BBB and significantly enhance precision delivery while concurrently reducing off-target drug release using temozolomide (TMZ) as a model.

2 Experimental

2.1 Materials

Unless otherwise specified, all chemicals were used as received from commercial sources without further purification. Soy L-α-phosphatidylcholine (Soy PC) was bought from Avanti Polar Lipids Inc. (AL, USA). 1,2-Distearoyl-sn-glycero-3-phosphoethanolamine with conjugated methoxyl poly(ethyleneglycol) (DSPE-$mPEG_{2000}$), 1,2-distearoyl-sn-glycero-3-phosphoethanolamine-N-[amino (polyethylene glycol)-2000] (DSPE-PEG_{2000}-NH_2) and 1,2-distearoyl-sn-glycero-3-phosphoethanolamine-N-[dibenzocyclooctyne (polyethylene glycol)-2000] (DSPE-PEG_{2000}-DBCO) were obtained from Xi'an Ruixi Biological Technology Co., Ltd. (Xi'an, China). 1-Ethyl-3-(3-dimethylaminopropyl) carbodiimide hydrochloride (EDC) and N-hydroxysuccinimide (NHS) were bought from Titan Scientific (Shanghai, China). Maltobionic acid (MA) and 4-carboxyphenylboronic acid were purchased from MERYER (Shanghai, China). Annexin V–fluorescein isothiocyanate (FITC)/propidium iodide (PI) apoptosis assay kit was obtained from Yeasen Biotechnology Co., Ltd. (Shanghai, China). TMZ was bought from InnoChem (Beijing, China). ICG and BAY-876 were purchased from MedChemExpress (USA). Methyl thiazolyl tetrazolium (MTT), Hoechst 33342, Alexa Fluor 488 5-Carboxamido-(Propargyl) (AF 488-Alkyne) and 1,1'-dioctadecyl-3,3,3',3'-tetramethylindodicarbocyanine (DiD) were purchased from Invitrogen (USA). Dulbecco's modified Eagle medium (DMEM) growth medium and fetal bovine serum (FBS) were purchased from Thermo Fisher Scientific Inc.

2.2 Preparation of DSPE-PEG-PBA and DSPE-PEG-MA

To prepare the Bioorthosome, we first synthesized DSPE-PEG-PBA, using DSPE-PEG_{2000}-NH_2 and 4-carboxyphenylboronic acid as starting materials. Specifically, 4-carboxyphenylboronic acid (83 mg, 0.5 mmol), 1-ethyl-3-(3-fimethylaminopropyl) carbodiimide hydrochloride (EDC) (191 mg, 1 mmol), and N-hydroxysuccinimide (NHS) (230 mg, 2 mmol) were dissolved in dimethylformamide (DMF) (20 mL) and stirred at room temperature for 30 min. Subsequently, 69 mg (0.03 mmol) of DSPE-PEG_{2000}-NH_2 was added to the reaction mixture. The reaction mixture was stirred for 24 h at room temperature and then the reaction system was dialysis (MWCO = 2000 Da) with DMF against water. The dialysis can thoroughly remove the compounds with a molecular weight lower than 2000 Da, and finally lyophilized to obtain DSPE-PEG-PBA. The products were confirmed by Matrix-Assisted Laser Desorption/Ionization Time of Flight Mass Spectrometry (MALDI-TOF MS) with Bruker Ultra-Flextreme and hydrogen nuclear magnetic resonance (^{1}H NMR) spectroscopy (Bruker AVANCE III HD 400 MHz NMR spectrometer).

Furthermore, DSPE-PEG-MA was synthesized by conjugating DSPE-PEG_{2000}-NH_2 and MA. Specifically, MA (179 mg, 0.5 mmol), EDC (191 mg, 1 mmol), and NHS (230 mg, 2 mmol) were

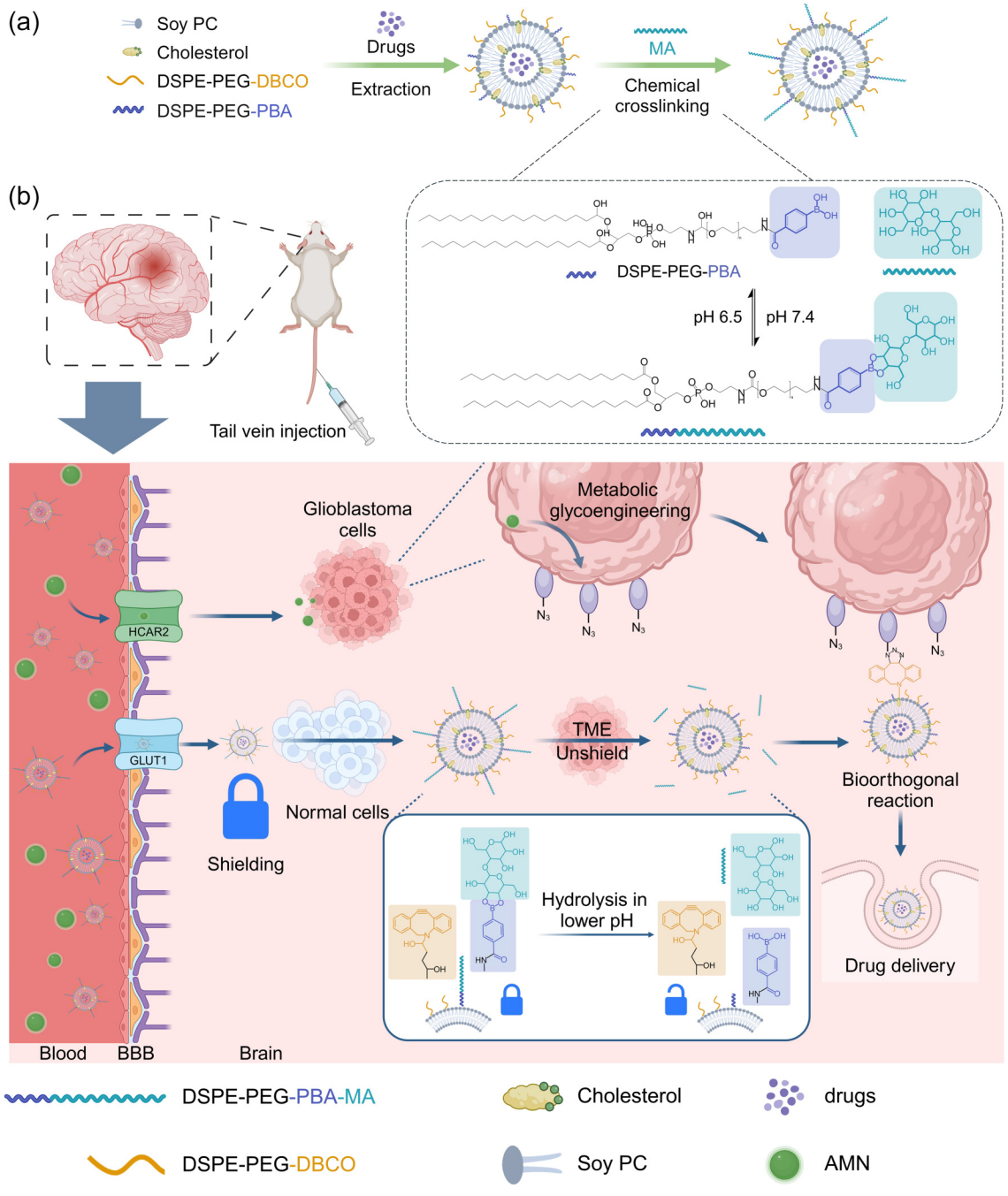

Scheme 1 Illustrative representation of the synthesis process and therapeutic strategy of Bioorthosome + AMN. (a) Fabrication of Bioorthosome and its pH-sensitive activation mechanism. (b) Targeted therapy for GBM involving the selective tumor tagging with AMN, followed by the traversal of the BBB by Bioorthosome for delivery. *In vivo* cell tagging with azides via AMN facilitates precise GBM targeting. Thereafter, Bioorthosomes navigate through healthy brain tissue to localize at the GBM lesion, where they are activated within the TME. This activation triggers a bioorthogonal reaction specifically at the tumor site, ensuring accurate drug delivery.

dissolved in DMF (20 mL) and stirred at room temperature for 30 min. Subsequently, 69 mg (0.03 mmol) of DSPE-PEG-NH_2 was added to the reaction mixture. The reaction mixture was stirred for 24 h at room temperature and then the reaction system was dialyzed (MWCO = 2000 Da) with water. Dialysis removes compounds with a molecular weight below 2000 Da, followed by lyophilizing to obtain DSPE-PEG-MA. The purpose of synthesizing DSPE-PEG-MA was to prepare liposomes with a non-detachable BBB-crossing ligand. The products were confirmed by MALDI-TOF MS with Bruker Ultra-Flextreme.

2.3 Preparation and characterization of AMN

The mannose derivative AMN was synthesized according to the synthetic routes detailed in Fig. S4 in the Electronic Supplementary Material (ESM). The structure details of the synthesized AMN were confirmed by electrospray ionization (ESI) mass spectrometry (Thermo LTQ XL Mass Spectrometer) and ^{1}H NMR spectroscopy (Bruker AVANCE III HD 400 MHz NMR spectrometer).

2.4 Preparation of the Bioorthosome

The Bioorthosome was prepared using the thin-film hydration

technique. Specifically, a mixture of 15 mg soy phosphatidylcholines (PC), 5 mg cholesterol, 0.6 mg DSPE-PEG_{2000}, 0.3 mg DSPE-PEG-PBA, and 0.1 mg DSPE-PEG-DBCO was dissolved in a methanol/chloroform solution (1:3, v/v) within a round-bottom flask. The solvent was evaporated using a rotary evaporator to form a thin lipid film on the flask's inner surface, followed by vacuum desiccation to ensure complete removal of residual solvents. The resulting lipid film was rehydrated with 4 mL of PBS containing 2 mg TMZ under ultrasonication. The rehydrated suspension was then passed 11 times through a polycarbonate membrane (200 nm) using an Avanti Mini-Extruder to obtain uniform liposomes. Thereafter, MA (20 mg, 0.06 mmol) was added to the liposome solution, which was subsequently incubated on a shaker overnight to promote the chemical reaction between PBA and MA. This resulted in the formation of pH-responsive borate ester bonds (PBA-MA), culminating in the synthesis of the final Bioorthosome. Control liposomes were synthesized employing the same methodology, specifically including the DBCO-MA Lipo, which is devoid of pH responsiveness and bioorthogonal chemistry shielding, as well as the DBCO-PBA Lipo, which lacks glucose functionality on its surface. For *in vitro* studies, rhodamine B (RhB) was encapsulated, while indocyanine green (ICG) was incorporated for *in vivo* biodistribution analysis across all liposome groups.

2.5 Characterization of Bioorthosome

The particle size, polydispersity index (PDI), and Zeta potential of Bioorthosome and the control liposomes were evaluated utilizing dynamic light scattering (DLS, Brookhaven NanoBrook Omni). The morphology of Bioorthosome was analyzed using transmission electron microscopy (TEM, 120 kV Talos L120C G2). The Bioorthosome suspension was loaded in a centrifugal dialysis tube (MWCO =10 kDa) and subjected to centrifugation at 3000 rpm for 10 min to remove the unencapsulated TMZ. The concentration of unencapsulated drugs was quantified via ultraviolet–visible (UV–vis) spectrophotometer (Shimadzu UV-1800), monitoring the absorption peak at 330 nm and correlating it with a pre-established standard curve. Encapsulation efficiency (EE%) was calculated using the formula: [(Drug added − unencapsulated drug)/Drug added] × 100%, while the drug loading content (DLC%) was determined as: [(Drug added − unencapsulated drug)/(Drug encapsulated + carrier)] × 100%.

2.6 Analysis of the formation of boronate ester bonds

Alizarin Red S (ARS) is a catechol dye that is non-fluorescent by itself, but it fluoresces upon binding to boronic acid. Therefore, ARS was utilized to validate the formation of boronate ester. Specifically, a mixture of ARS (0.3 mM) and DSPE-PEG-PBA (5 μM) was prepared with varying concentrations of MA (0–40 μM). In this system, MA competes with ARS for binding to DSPE-PEG-PBA and leads to quenching of ARS fluorescence. The changes in ARS fluorescence intensity were detected using a Shimadzu FL-6500 fluorescence spectrophotometer at excitation wavelength 468 nm and emission wavelength 585 nm.

2.7 *In vitro* stability and drug release

The suspension of Bioorthosome@TMZ in PBS was maintained at room temperature, and the size distribution along with the PDI was assessed using DLS on a daily basis for a duration of two weeks. All measurements were performed in triplicate to ensure accuracy and reliability. In order to evaluate the *in vitro* drug release kinetics, Bioorthosome@TMZ was placed inside dialysis bags with an MWCO of 1500 Da and immersed in 50 mL PBS at pH 7.4 and pH 5.0, mimicking physiological and tumor microenvironment conditions, respectively. At each time point, 1 mL of PBS was taken out and replaced with 1 mL of fresh PBS to maintain system conditions. The drug concentrations in the collected samples were quantified using UV–vis spectrophotometry, with established standard curves employed to calculate cumulative release amounts. Each pH condition was tested with three independent experimental replicates.

2.8 Hemolytic test of Bioorthosome@TMZ

Blood samples were collected from the retro-orbital venous plexus of C57BL/6 mice and transferred into ethylenediaminetetraacetic acid (EDTA) tubes to prevent coagulation. Red blood cells (RBCs) were separated via centrifugation and washed five times with PBS for purification. The RBCs were then diluted with saline to achieve a 2% (v/v) hematocrit. To assess hemolysis, 500 μL of RBC suspension was mixed with 500 μL of Bioorthosome@TMZ at varying concentrations (1 mM, 500 μM, 250 μM, 125 μM, 62.5 μM). A saline solution was used as a negative control, while 1% Triton X-100 served as the positive control. After incubating the mixtures at 37 °C for 2 h, the samples were centrifuged at 5000 rpm for 6 min. Hemolysis was visually inspected, and the absorbance of the supernatant was measured at 540 nm using a microplate reader. Hemolysis (%) was calculated using the formula: Hemolysis (%) = (As − Ab)/(Ac − Ab) × 100%. As is the absorbance of the sample, Ac is the absorbance of Triton-X 100, and Ab is the absorbance of PBS.

2.9 Cell culture

GL261-Luc and bEnd.3 cell lines were obtained from Ubigene Biosciences (Guangzhou, China). The bEnd.3 and GL261-Luc cell lines were grown in Dulbecco's modified Eagle medium (DMEM) supplemented with 10% fetal bovine serum (FBS), 1% (v/v) penicillin/streptomycin. For GL261-Luc selection, the medium was additionally supplemented with 1 μg/mL puromycin. Both cells were cultured at 37 °C under a 5% CO_2 environment.

2.10 *In vitro* detection of azides on cells

GL261-Luc cells were seeded in confocal culture dishes (1×10^4 cells/well) and incubated for 12 h to allow adherence. Following this, AMN was added to achieve a final concentration of 50 μM. After a 24 h incubation, the cells were sequentially stained with Hoechst 33342 for 15 min, DiD for 15 min and AF 488-Alkyne for 30 min, respectively. Excess dye was removed by washing cells with PBS (twice). Imaging was subsequently conducted using Leica STELLARIS 5 confocal laser scanning microscope (CLSM).

2.11 Cellular uptakes of different formulations of liposomes

To investigate whether the PBA-MA structure on the surface of the Bioorthosome exerts a shielding effect on DBCO and whether the bioorthogonal reaction enhances the targeting capability of the liposomes, GL261-Luc cells were seeded in a confocal culture dish and allowed to adhere. Subsequently, RhB-loaded liposomes with various surface modifications were added to the culture dish. Cells were treated with 50 μM AMN for 8 h incubation, then stained with Hoechst 33342 for 15 min. After the staining, the cells were

washed twice with PBS to remove any excess dye, and imaged by CLSM.

2.12 Lysosome colocalization

RhB was employed as a fluorescent surrogate for the therapeutic agent, enabling real-time tracking of Bioorthosome@RhB within cellular environments. GL261-Luc cells were seeded in glass-bottom culture dishes and cultured overnight. Following a 6-h incubation with Bioorthosome@RhB, the cells underwent thorough washing with PBS to remove unbound particles. Lysosomes were subsequently stained with LysoTracker™ Green for 15 min, while nuclear staining was performed using Hoechst 33342 for 15 min. The stained cells were washed twice with PBS before being imaged via CLSM.

2.13 Cell viability of Bioorthosome@TMZ in the GBM cell line

GL261-Luc cells were seeded in a 96-well plate and incubated for 12 h to allow cell adhesion. Then, varying concentrations of Bioorthosome@TMZ + AMN (fixed at 50 μM), Bioorthosome@TMZ, free TMZ, and Bioorthosome (without TMZ) were incubated with cells for 24 h. To assess cell viability, 100 μL of MTT solution (5 mg/mL) was added to each well and incubated for an additional 4 h. The medium was then discarded, and 150 μL of DMSO was added to dissolve the formazan crystals. The plate was incubated at 37 °C for 15 min, and absorbance was measured at 570 nm using a microplate reader (Synergy LX from Biotek). Cell viability was calculated using the following formula: Cell viability = Absorbance of samples/Absorbance of blank control × 100%.

2.14 Cell apoptosis induced by Bioorthosome@TMZ

To further explore the apoptotic potential of Bioorthosome@TMZ, GL261-Luc cells were seeded in 6-well plates (1×10^5 cells/well) and allowed to adhere for 12 h. Afterward, Bioorthosome@TMZ + AMN and other control groups (the equivalent concentration of TMZ is 50 μM) were added and incubated for 24 h. The GL261-Luc cells were then harvested and stained with Annexin V–FITC/PI for analysis by flow cytometry. Apoptosis was detected on the BD Fortessa X20 flow cytometer (Becton Dickinson, USA).

2.15 Establishment of an *in vitro* BBB Transwell model

To explore the GLUT1-mediated BBB-crossing of Bioorthosome, we utilized a Transwell cell culture system to mimic the structure and function of BBB. In detail, bEnd.3 cells were seeded in the upper chamber of a Transwell insert (pore size 0.4 μm) and cultured until the trans-endothelial electrical resistance (TEER) surpassed 200 $\Omega \cdot cm^2$, indicating the establishment of tight junctions that closely mimic the integrity of the BBB. Simultaneously, GL261-Luc cells were plated in the lower chamber and allowed to adhere overnight.

2.16 *In vitro* evaluation of BBB penetration

To evaluate the BBB-crossing potential of AMN, a concentration of 50 μM AMN was introduced into the upper chamber of a transwell model of BBB and incubated for 48 h. Subsequently, the cells were sequentially stained with Hoechst 33342 for 15 min and AF 488-Alkyne for 30 min. Excess dye was removed by washing cells with PBS (twice). Imaging was subsequently conducted using CLSM to indicate metabolized azides resulting from AMN treatment.

To investigate the BBB-crossing ability of Bioorthosome, 100 μL of Bioorthosome@RhB and DBCO-PBA Lipo@RhB were respectively added to the upper chamber of the BBB Transwell model. At different time points, 200 μL of medium was collected from the lower chamber as a sample, and an equal volume of fresh medium was replenished. The fluorescence intensity of the collected samples was measured for quantification, and permeability was calculated based on the initially added amount.

2.17 Validation of GLUT1-mediated BBB-crossing

To confirm whether GLUT1 mediates the translocation of Bioorthosome@RhB across the BBB, we treated bEnd.3 cells in the *in vitro* BBB model with the GLUT1 inhibitor BAY-876 (50 nM) for 24 h. Following this treatment, Bioorthosome@RhB was introduced into the upper chamber, and at the 24 h time point, 100 μL samples were collected from both the upper and lower chambers to measure fluorescence intensity. This allowed us to evaluate the relationship between GLUT1 expression and the ability of Bioorthosome@RhB to traverse the BBB.

2.18 Establishment of *in situ* GBM model

All experimental procedures were conducted in accordance with the guidelines set by the Animal Use and Care Administrative Advisory Committee of Shanghai Jiao Tong University (Approval Number: A2024180). C57BL/6 mice (male, 6 weeks old, weighing 18–20 g) were procured from GemPharmatech Co., Ltd. (Nanjing, China) and housed in a specific pathogen-free (SPF2) environment provided by the Laboratory Animal Center of Shanghai Jiao Tong University. The method for establishing an orthotopic GBM model involved using a stereotactic frame to inject 3×10^5 GL261-Luc cells (5 μL) into the right side of the bregma, 1.5 mm lateral, 2 mm anterior, and 3.3 mm deep. On the 3rd day after injection, tumor formation was confirmed by intraperitoneal injection of d-luciferin potassium salt (150 mg/kg) followed by *in vivo* imaging systems (IVIS, PerkinElmer, USA).

2.19 Evaluation of *in vivo* BBB transportability and glioma targeting

To evaluate the biodistribution and GBM-targeting efficacy of the formulations *in vivo*, the fluorescent dye ICG was encapsulated into common liposome (Lipo@ICG), DBCO-MA Lipo (DBCO-MA Lipo@ICG), and Bioorthosome (Bioorthosome@ICG). On the 10th day post-tumor implantation, mice were administered an equivalent dose of 1 mg/kg ICG via tail vein across different treatment groups. Whole-body imaging was performed at various time points using IVIS. After imaging, the mice were euthanized, and the major organs (brain, heart, liver, spleen, lungs, kidneys) were collected for *ex vivo* imaging to further assess tissue distribution. The brain tissues were embedded in optimal cutting temperature compound (OCT) for frozen sectioning, and CLSM was employed to capture detailed images of the GBM and surrounding brain tissue.

2.20 Evaluation of the anti-tumor effect on GBM

On the 3rd day after tumor inoculation, once significant bioluminescence signals were detected via the IVIS, the mice were randomly allocated into 6 groups: saline, free TMZ, DBCO-PBA Lipo@TMZ + AMN, DBCO-MA Lipo@TMZ + AMN, Bioorthosome@TMZ, and Bioorthosome@TMZ + AMN. For the first three days of the treatment, mice in the DBCO-PBA Lipo@TMZ + AMN, DBCO-MA Lipo@TMZ + AMN, and

Bioorthosome@TMZ + AMN groups received daily tail vein injections of AMN at a dose of 5 mg/kg. Starting on day 4 and continuing until day 13, treatments were administered every three days via tail vein injection with equivalent doses of 5 mg/kg TMZ. Throughout treatment, tumor growth was monitored by assessing bioluminescence signals using the IVIS. Simultaneously, body weight and survival rates were recorded at regular intervals. At the endpoint of the study, the brain and other major organs were collected for hematoxylin-eosin (HE) staining to evaluate the anti-tumor efficacy of the different treatments. Furthermore, immunofluorescence staining for terminal deoxynucleotidyl transferase dUTP nick end labeling (TUNEL) was performed to assess proliferative changes in the tumor tissue, providing additional insights into therapeutic impact.

2.21 *In vivo* detection of azides

Brain cryosection from mice treated with AMN were stained with Hoechst 33342 (15 min) to visualize nuclei, followed by AF 488-Alkyne (30 min) to indicate azide-containing sialylations in the tumor region. Excessive dye was washed off twice with PBS. Imaging was subsequently performed using CLSM.

2.22 Statistical analysis

Data and statistical analysis were conducted using GraphPad Prism version 9.5.1. For comparisons between two experimental groups, statistical significance was determined using two-tailed Student's t-tests. In experiments involving multiple groups, either one-way or two-way ANOVA with Tukey's post-hoc correction was applied to assess differences across the groups. Survival analysis was performed using the log-rank (Mantel-Cox) test. Results were considered statistically significant based on the following *P*-values: ns (not significant), $*P < 0.05$, $**P < 0.01$, $***P < 0.001$, and $****P < 0.0001$.

3 Results and discussion

3.1 Preparation and characterization of Bioorthosome and AMN

First, the building blocks of the Bioorthosome were prepared. As shown in Fig. S1 in the ESM, DSPE-PEG-PBA was synthesized and characterized by MALDI-TOF MS and ^{1}H NMR (Figs. S2 and S3 in the ESM) to confirm the successful synthesis. The AMN was obtained through the synthetic routes shown in Fig. S4 in the ESM, and verified by electrospray ionization mass spectrometry (ESI-MS) (Fig. S5 in the ESM) and ^{1}H NMR (Fig. S6 in the ESM). To construct Bioorthosome, a DBCO-PBA dual-functionalized liposome (DBCO-PBA Lipo) was prepared by incorporating DSPE-PEG-PBA and DSPE-PEG-DBCO (purchased from commercial source), followed by adding MA to react with PBA via borate ester bonds, resulting in the final Bioorthosome with a DBCO surface that was shielded by BBB-crossing MA. The successful MA modification was validated by testing the changes in surface charge. As shown in Fig. 1(a), the Zeta potential of the DBCO-PBA Lipo evidently decreased due to the introduction of MA, suggesting the successful installation of MA on the surface. To further confirm the formation of boronate ester bonds between PBA and MA, an ARS-based fluorescence assay was employed. At an excitation wavelength of 468 nm, the fluorescence intensity of ARS gradually decreased as the concentration of MA increased from 0 to 40 μM, confirming the formation of boronate ester between MA and PBA (Fig. 1(b) and Fig. S7 in the ESM). The morphology of both DBCO-PBA Lipo and Bioorthosome were observed via TEM (Figs. 1(c) and 1(d)). Dynamic light scattering (DLS) analysis revealed that the DBCO-PBA Lipo and Bioorthosome had a hydrodynamic diameter of 124.5 and 125.7 nm with a PDI of 0.156 and 0.123, respectively (Figs. 1(c) and 1(d)). The Bioorthosome remained stable in size and PDI for 14 days at room temperature (Fig. 1(e)). Then, the first-line anti-GBM drug, TMZ, was loaded and resulted in a Bioorthosome@TMZ. By calculation, the encapsulation and drug loading efficiency of the Bioorthosome@TMZ were determined as 79.66% and 6.93%, respectively. Then, the drug releasing profile of Bioorthosome@TMZ was investigated by using acidic stimulation. As shown in Fig. 1(f), only approximately 16% of TMZ was released from Bioorthosome@TMZ over a period of 24 h. In contrast, acidic pH (5.0) stimulation resulted in the release of about 83% of TMZ within the same time frame. These results indicate that Bioorthosome would efficiently release the payloads in lysosomal pH while minimizing premature release in the bloodstream.

DBCO-PBA Lipo, lacking MA on its surface, was used in subsequent experiments to verify that MA can facilitate BBB translocation via GLUT1. To emphasize the importance of the locked bioorthogonal chemistry, DSPE-PEG-MA was additionally synthesized (Figs. S8 and S9 in the ESM) to prepare a control liposome (DBCO-MA Lipo) possessing "always-on" DBCO moieties and BBB-crossing MA ligands (Table S1 in the ESM). The DBCO-MA Lipo showed a hydrodynamic size of 118 nm with a PDI of 0.131 (Fig. S10 in the ESM). The morphology of DBCO-MA Lipo was observed via TEM (Fig. S10 in the ESM). DSPE-PEG-MA exhibited a comparable molecular length to DSPE-PEG-DBCO, allowing for the integration of undetachable BBB-crossing MA ligands onto the liposome while maintaining the bioorthogonal reaction between DBCO and azide-containing sialylations on cell surfaces.

3.2 Lysosome co-localization of the Bioorthosome

To further confirm whether the Bioorthosome is transported into lysosomes and releases its payload within the acidic lysosomes, we examined the lysosomal co-localization of the Bioorthosome. To make the encapsulated drug detectable, Rhodamine B (RhB) was employed as a fluorescent surrogate. The Bioorthosome@RhB was incubated with GBM cell line (GL261-Luc), and its intracellular distribution was visualized using CLSM. Lysosomes were labeled with LysoTracker. As depicted in Fig. 2(a), the Bioorthosome@RhB was efficiently internalized by GBM cells, as evidenced by the red fluorescence of RhB. The intracellular localization of RhB suggested that the Bioorthosome@RhB exhibited significant co-localization with lysosomes between 2 and 4 h, which separated from lysosome by 6 h post-incubation (Fig. 2(b)). These observations suggested that the Bioorthosome was capable of releasing its payload within lysosomes and subsequently distributed the payload beyond the lysosomal compartment over time.

3.3 Cellular uptake of Bioorthosomes

Initially, we cultured cells with 50 μM AMN, followed by the introduction of an AF488-labeled alkyne via bioorthogonal chemistry to validate the effectiveness of metabolic glycoengineering [36, 37]. As depicted in Fig. 2(c), cells treated with AMN exhibited robust fluorescence upon AF488 labeling, precisely

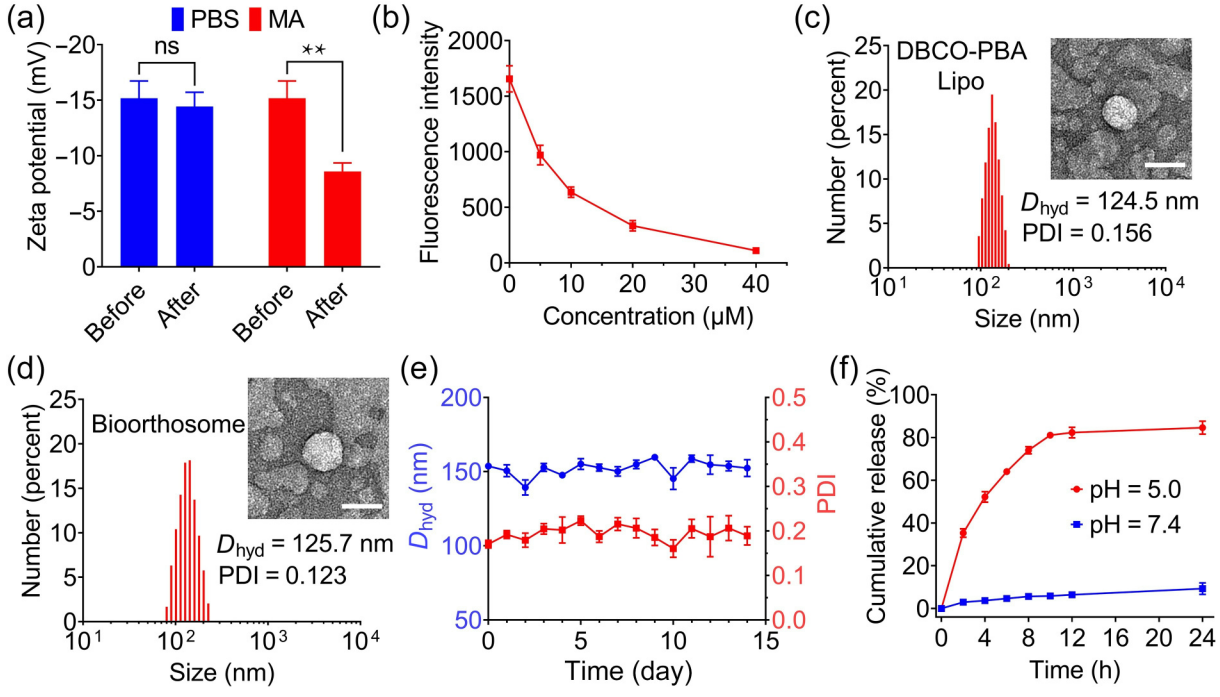

Figure 1 Bioorthosome characterization. (a) Surface charge dynamics (n = 3) of DBCO-PBA Lipo following the addition of PBS or MA. (b) Fluorescence assay employing ARS as an indicator verified the formation of boronate esters between PBA and MA (n = 3). TEM images and size distributions for (c) DBCO-PBA Lipo and (d) Bioorthosome, with a scale bar denoting 100 nm. (e) Assessment of Bioorthosome stability through DLS measurements (n = 3). (f) pH-dependent cumulative release profile of TMZ from Bioorthosome (n = 3).

colocalizing with the cell membrane (Fig. 2(d)), thereby confirming the efficacy of our AMN-based metabolic glycoengineering.

To assess the influence of incorporating bioorthogonal reactions and the effect of PBA-MA shielding of DBCO on the targeting efficiency of the Bioorthosome, GL261-Luc cells were incubated with various formulations for 24 h, including Bioorthosome@RhB + AMN, and its control treatments: DBCO-PBA Lipo@RhB + AMN and Bioorthosome@RhB (azide was blocked). A common liposome (Lipo@RhB) was additionally added as positive control. The CLSM results (Figs. 2(e) and 2(f)) revealed that Bioorthosome@RhB showed similar intracellular signal comparing to Lipo@RhB due to the absence of bioorthogonal reaction moieties. Notably, the treatment with DBCO-PBA Lipo@RhB + AMN, which lacked MA shielding for the bioorthogonal reaction, showed the highest level of cellular uptake compared to the other three groups, indicating that the bioorthogonal reaction significantly enhances lysosomal uptake. As expected, the uptake efficiency of Bioorthosome@RhB + AMN was relatively low due to the MA shielding effect to DBCO, which preserved the capacity for bioorthogonal reactions. These findings underscored the importance of bioorthogonal targeting in our Bioorthosome system and confirmed that the PBA-MA structure effectively shields the DBCO on the surface of the Bioorthosome, consequently minimizing off-target interactions and refining the precision of drug delivery.

3.4 Cell viability and apoptosis induction ability of Bioorthosome

We encapsulated TMZ within Bioorthosome to evaluate its *in vitro* antitumor efficacy. Initially, the Bioorthosome@TMZ and control materials was incubated with AMN pretreated GL261-Luc GBM cells for 24 h, followed by assessment using the MTT assay. As illustrated in Fig. 2(g) and Fig. S11 in the ESM, the IC50 for the Bioorthosome@TMZ + AMN group was determined to be 41.58 μM, while the IC50 for Bioorthosome@TMZ alone was 222.3 μM. Furthermore, the Bioorthosome treatment, which did not contain any encapsulated drug, showed no significant impact on cell viability, indicating that our Bioorthosome possess good biocompatibility. These findings highlight that the incorporation of bioorthogonal reactions significantly enhances the delivery efficacy of encapsulated drugs—approximately 5.3 times greater than without such modifications—demonstrating the substantial potential of this delivery platform for practical applications.

We further investigated the apoptotic effects of the Bioorthosome on GL261-Luc cells using flow cytometry. The results revealed that the Bioorthosome@TMZ + AMN induced the highest level of apoptosis among all tested conditions (Figs. 2(h) and 2(i)). Specifically, the percentage of apoptotic cells in the Bioorthosome@TMZ + AMN group was 30.14% ± 3.67%, which was significantly higher than that observed for Bioorthosome@TMZ (21.74% ± 1.34%) and Free TMZ (16.30% ± 1.75%). Additionally, the apoptotic rates in the empty Bioorthosome did not differ significantly from the control group, consistent with the cytotoxicity results. In summary, the above results demonstrate that our bioorthogonal reaction-based GBM-targeting delivery platform, Bioorthosome@TMZ + AMN, demonstrates excellent targeting capabilities and biocompatibility, offering considerable promise for GBM treatments.

3.5 *In vitro* evaluation of BBB penetration

We evaluated the BBB-crossing capability of Bioorthosomes using an *in vitro* BBB model established with bEnd.3 cells. As shown in Fig. 3(a), bEnd.3 cells were seeded in the upper chamber of a Transwell system where they formed tight junctions, while GL261-

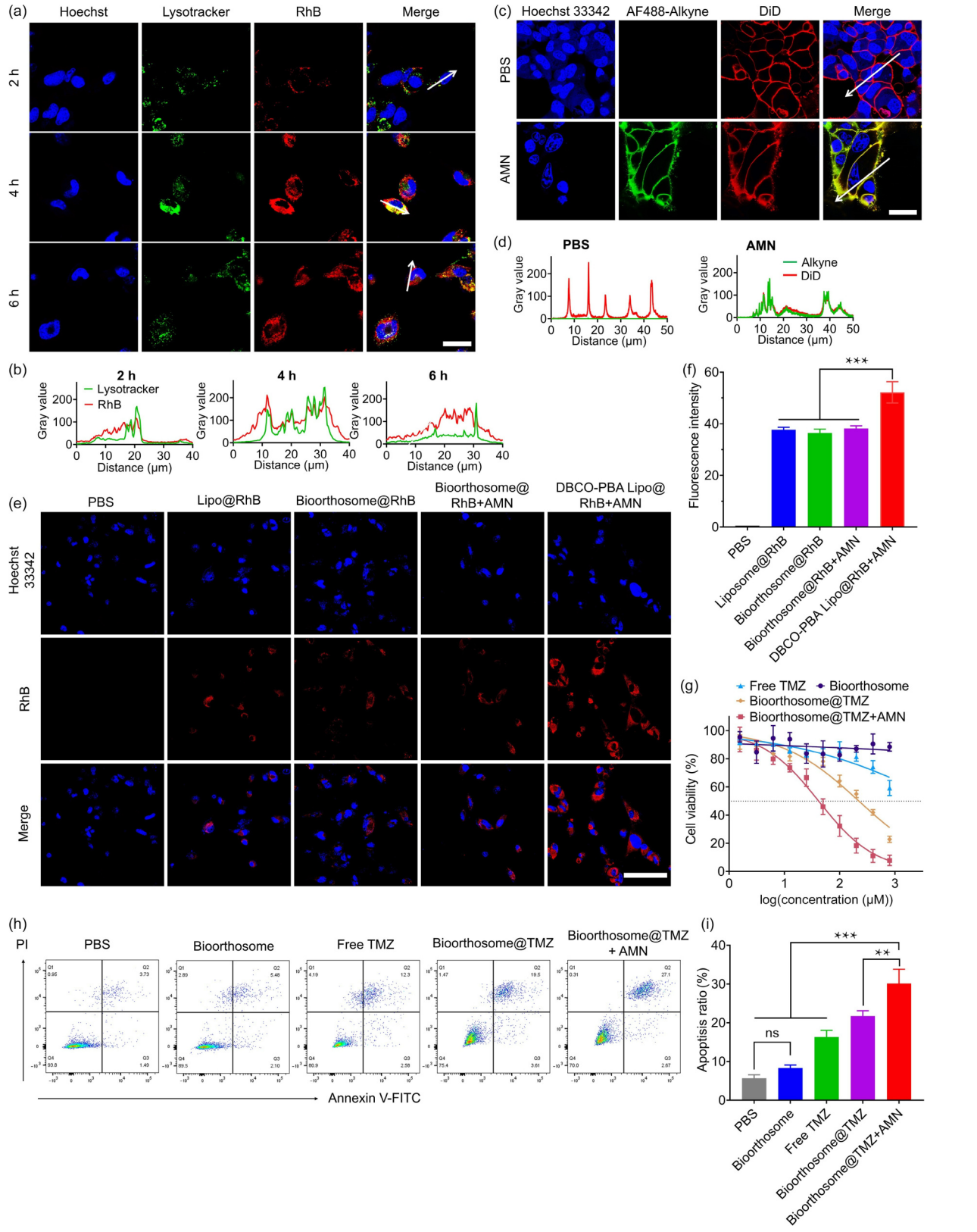

Figure 2 *In vitro* efficacy of Bioorthosome. (a) CLSM images depicting the co-localization of Bioorthosome with lysosomes, with lysosomes stained by LysoTracker Green. Scale bar: 30 μm. (b) Gray level analysis of the green and red channels, along with white solid lines on the merged fluorescence images, illustrating co-localization in (a). (c) CLSM images of cellular uptake and *in situ* modification of AMN within GL261-Luc cells. Scale bar: 20 μm. (d) Gray level analysis of the green and red channels, with white solid lines on the merged fluorescence images, showing co-localization in (c). (e) Effect of various formulations on cellular uptake, with a scale bar representing 100 μm. (f) Quantitative analysis (n = 3) of the RhB fluorescence signal from (e). (g) MTT assay results indicated GL261 cell viability after different treatments (n = 3). (h) Flow cytometry analysis of apoptosis in GL261-Luc cells. (i) Quantitative analysis (n = 3) of apoptosis and necrosis rates in GL261-Luc cells based on (h).

Luc cells were cultured in the lower chamber. RhB was encapsulated into Bioorthosome and other control liposomes to serve as a tracer, allowing us to assess their ability to traverse BBB. The RhB-loaded liposomes were added to the upper chamber, and fluorescence intensity in the lower chamber was monitored over time to evaluate the time-dependent BBB-crossing efficiency.

As depicted in Figs. 3(b) and 3(c), the Bioorthosome@RhB exhibited a markedly superior BBB-crossing efficiency when compared to the DBCO-PBA Lipo@RhB, indicating that the MA surface substantially enhances the liposome's ability to traverse the BBB. To examine whether the DBCO and PBA surface modifications also contribute to the BBB permeability, we utilized a liposome with a conventional PEG surface (Lipo@RhB). The translocation rate of the DBCO-PBA Lipo@RhB showed no significant difference from that of the Lipo@RhB, implying that the modifications with DBCO and PBA surfaces do not augment the liposome's capacity for BBB penetration. To further investigate the role of GLUT1 in the transcytosis process, we added a GLUT1 inhibitor (BAY-876) to the upper chamber to competitively bind the GLUT1 and blunt the GLUT1-mediated transcytosis [38, 39]. The results demonstrated a marked reduction in the migration efficiency of Bioorthosome@RhB following the addition of the inhibitor (Fig. 3(d)), underscoring the crucial role of GLUT1-mediated transcytosis in facilitating Bioorthosome's BBB crossing. Additionally, we confirmed the BBB penetration capability of AMN. The CLSM results showed that after the addition of AMN to the upper chamber, the cells in the lower chamber exhibited azide modification on their surface, indicating that AMN can effectively cross the BBB (Fig. 3(e)). These characteristics further highlight the potential of Bioorthosome as a targeted delivery system for brain tumors.

3.6 Enhanced targeted delivery of Bioorthosome

To evaluate the tumor-targeting efficacy and biodistribution of our Bioorthosome, we established an orthotopic GBM mouse model via intracranial injection of GL261-Luc cells. A near-infrared (NIR) fluorescent dye ICG was employed as a surrogate to trace various liposome formulations *in vivo*. Different liposome formulations were administered via tail vein injection into orthotopic GBM mice, followed by monitoring of ICG fluorescence at multiple time points. As illustrated in Fig. 4(a) and Fig. S12 in the ESM, Bioorthosome@ICG + AMN demonstrated significantly enhanced brain fluorescence and prolonged retention compared to the control groups, reaching a peak at 8 h with maximal accumulation in the brain. In contrast, the DBCO-MA Lipo@ICG + AMN treatment exhibited lower GBM accumulation than Bioorthosome@ICG + AMN, indicating that the presence of both moieties may interfere with their respective biological functions. The Bioorthosome@ICG showed reduced accumulation due to the absence of azide metabolized on the GBM cell surface. Meanwhile, Lipo@ICG displayed the lowest signal in the mouse head, attributed to its inability to cross the BBB. The quantitative analysis (Fig. 4(b)) demonstrates that, between 2 to 24 h post-administration, the fluorescence intensity of the Bioorthosome@ICG + AMN formulation was significantly higher than that of the two control groups lacking the bioorthogonal reaction. Furthermore, between 8

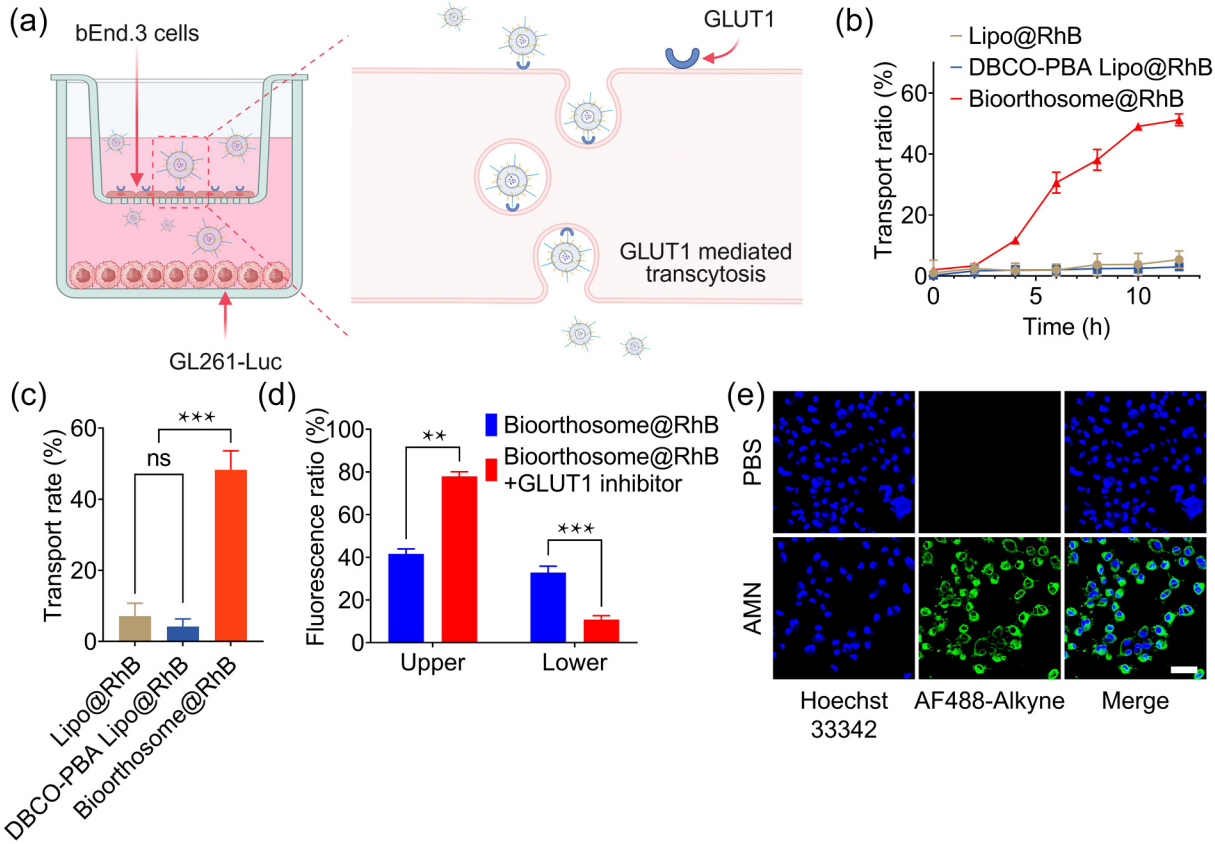

Figure 3 *In vitro* BBB penetration of Bioorthosome. (a) Schematic depiction of the GLUT1-mediated BBB crossing process on the surface of bEnd.3 cells using an *in vitro* transwell model. (b) Time-dependent BBB-penetration of Bioorthosome (n = 3). (c) Transporting rate of Bioorthosome at the 12-h time point. (d) Influence of GLUT1 on the BBB crossing efficiency of Bioorthosome (n = 3). (e) Demonstration of BBB crossing capability of AMN, indicated by AF488-Alkyne. Scale bar: 50 μm.

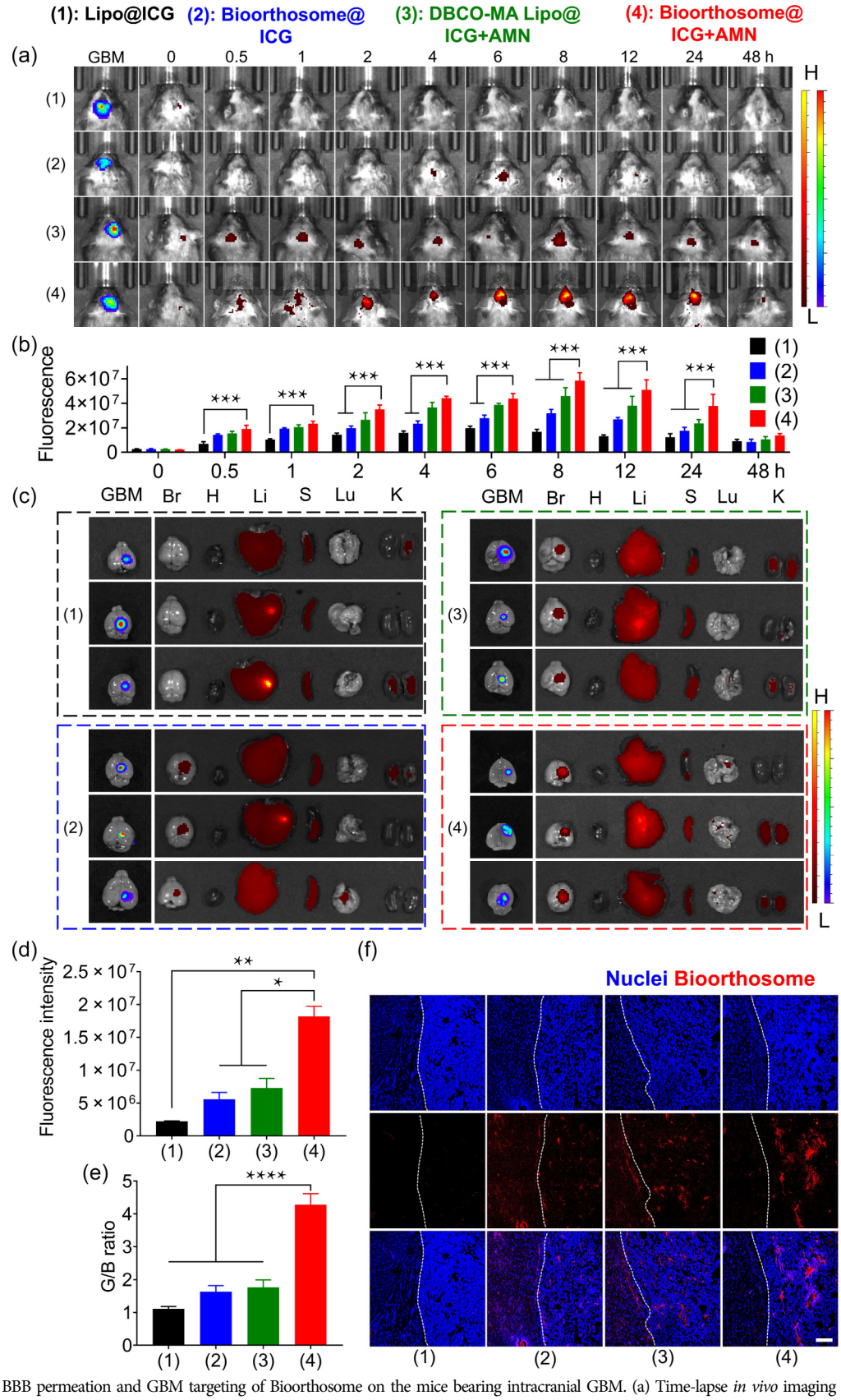

Figure 4 *In vivo* BBB permeation and GBM targeting of Bioorthosome on the mice bearing intracranial GBM. (a) Time-lapse *in vivo* imaging of GL261-Luc GBM-bearing mice post-injection with ICG-labeled liposomes. (b) Quantitative analysis of *in vivo* imaging data at various time points following tail vein injection (n = 3). (c) *Ex vivo* mapping of liposome distribution in GBM-bearing mice (n = 3). (d) Measurement of ICG fluorescence intensity in the brain tissue *ex vivo* (n = 3). (e) Ratio of fluorescence signal intensity at the GBM site to that of normal brain tissue (G/B ratio) (n = 3). (f) Fluorescence microscopy images of brain sections from GL261-Luc GBM-bearing mice after intravenous administration of various liposome formulations. Scale bar: 100 μm.

to 24 h, a pronounced difference in fluorescence intensity was observed between Bioorthosome + AMN and DBCO-MA Lipo + AMN. The quantitative data indicate that the incorporation of the bioorthogonal reaction significantly enhances both the duration and amount of drug accumulation within GBM tissues. Additionally, the pH-responsive detachment of the MA component in Bioorthosome may also prevent reverse translocation across the BBB, thereby facilitating more sustained and tumor-specific retention [13].

Following the final *in vivo* imaging session, the mice were euthanized, and organs were harvested for *ex vivo* imaging (Fig. 4(c)). Despite the liver and spleen's critical role in filtering blood circulation, *ex vivo* imaging revealed significant fluorescence accumulation of Bioorthosome + AMN in the GBM regions, with intensity markedly exceeding that of the control groups (Fig. 4(d)). To evaluate the specificity of GBM targeting, we introduced the G/B ratio, calculated by dividing the fluorescence signal at the GBM site by that in normal brain tissue [13]. The results demonstrate that the Bioorthosome + AMN group exhibits a significantly higher ratio compared to other groups (Fig. 4(e)). To further verify that the PBA-MA on the Bioorthosome surface effectively reduces off-target drug release by shielding DBCO, we performed histological sectioning of the harvested brains and used CLSM to assess ICG distribution in tumor and normal tissues (Fig. 4(f)). The results indicate that the Bioorthosome@ICG + AMN group showed the highest overall fluorescence intensity, while the DBCO-MA Lipo@ICG + AMN and Bioorthosome@ICG groups also demonstrated notable infiltration in the brain, consistent with the *ex vivo* imaging findings. Notably, both the Bioorthosome@ICG and DBCO-MA-Lipo + AMN groups exhibited nonspecific distributions in normal brain tissues due to the absence of bioorthogonal targeting and pH-responsive shielding, whereas the Bioorthosome + AMN group displayed fluorescence strictly within the confined tumor region, leveraging the benefits of our locked bioorthogonal strategy.

Additionally, the *in vivo* AMN metabolism and bioorthogonal chemistry-mediated GBM targeting of the Bioorthosome + AMN group were investigated using CLSM. As illustrated in Fig. S13 in the ESM, CLSM results revealed that the azides generated by AMN were present in both GBM and normal cells. Notably, the Bioorthosome exhibited minimal off-target distribution, despite the presence of azide labeling in normal cells. These findings confirm the critical role of the PBA-MA shielding mechanism and its pH-responsive unshielding, which ensures precise and targeted drug delivery. Consequently, the Bioorthosome + AMN system not only effectively delivers drugs to GBM sites but also achieves precise targeting by responding to the tumor microenvironment.

3.7 *In vivo* therapeutic efficacy of Bioorthosome on orthotopic GBM model

To further assess the enhanced delivery efficacy of our Bioorthosomes, an orthotopic GBM mouse model was created by intracranial inoculation of GL261-Luc cells, followed by administration of Bioorthosome-mediated chemotherapy. Following confirmation of GBM development through bioluminescence imaging, the mice were randomly assigned to one of six treatment cohorts: Saline control, Free TMZ, DBCO-PBA Lipo@TMZ + AMN, DBCO-MA Lipo@TMZ + AMN, Bioorthosome@TMZ, and Bioorthosome@TMZ + AMN. In this setup, the Bioorthosome@TMZ group was included to underscore the significance of the AMN-based glycoengineering, while the DBCO-MA Lipo@TMZ + AMN group was used to highlight the switchable bioorthogonal reaction. The DBCO-PBA Lipo@TMZ + AMN group was designed to demonstrate the BBB-crossing capability of the MA modification. The inclusion of free TMZ allowed for a direct comparison with the Bioorthosomes, thereby emphasizing the advantages of liposomal drug delivery. Following the treatment protocol (Fig. 5(a)), mice in the three AMN-treating groups received tail vein injections of 5 mg/kg AMN for the first three days. From day 4 to 15, treatment was administered to each group every three days with TMZ (5 mg/kg). Tumor progression was monitored via IVIS (Fig. 5(b)), and bioluminescence intensity was quantified (Fig. 5(c)). Among all the treatments, the Bioorthosome@TMZ + AMN group demonstrated the highest GBM inhibiting efficiency, as it can cross BBB and responsively switch the ligands from BBB-crossing moieties to GBM-targeting DBCO in TME. In comparison, Bioorthosome@TMZ showed reduced efficacy compared to Bioorthosome@TMZ + AMN, attributable to the absence of azide modification on the GBM cell surface, thereby confirming the bioorthogonal reaction's pivotal role in our targeting approach. The DBCO-MA Lipo@TMZ + AMN group demonstrated a diminished anti-GBM effect compared to Bioorthosome@TMZ + AMN, underscoring the significance of the DBCO ligands on the liposome's surface. The DBCO-PBA Lipo@TMZ + AMN was ineffective in inhibiting intracranial GBM due to its inability to efficiently cross the BBB. Notably, all treatments, with the exception of Bioorthosome@TMZ + AMN, exhibited inferior efficacy to free TMZ, indicating that efficient drug delivery is crucial for GBM treatment. The Bioorthosome also significantly improves the overall survival of the mice bearing intracranial GBM. As shown in Fig. 5(d), the median survival of mice treated with Bioorthosome@TMZ + AMN was extended by 29.2% compared to the saline group, 26.2% compared to Bioorthosome alone, and 12.7% compared to DBCO-MA Lipo@TMZ + AMN. Additionally, body weight loss of free TMZ treatments was significantly mitigated in the Bioorthosome@TMZ group + AMN (Fig. 5(e)). Brain tissue sections further validated the superior antitumor efficacy of Bioorthosome@TMZ + AMN. Additionally, we assessed tumor cell apoptosis using TUNEL immunofluorescence staining to evaluate the pro-apoptotic effect (Figs. 5(f) and 5(g)). The Bioorthosome@TMZ + AMN group showed significantly enhanced fluorescence compared to the other groups, indicating a stronger pro-apoptotic effect. The histopathological images of whole brains (Fig. 5(h)) further revealed that the Bioorthosome@TMZ + AMN treatment extensively retarded the GBM progression in the brain, showing the best efficacy than all the other treatments.

3.8 Biocompatibility of the Bioorthosome

The histopathological analysis and hemolysis were applied to investigate the biocompatibility of our Bioorthosome. As shown in Fig. S14 in the ESM, the major organs, including heart, liver, spleen, lung and kidneys, did not exhibit abnormality, comparing to the saline-treated mice. Furthermore, the Bioorthosome showed no evidence to cause hemolysis (Fig. S15 in the ESM). These results collectively confirm the good biocompatibility of the Bioorthosome.

4 Conclusions

In this study, we developed a Bioorthosome designed to effectively

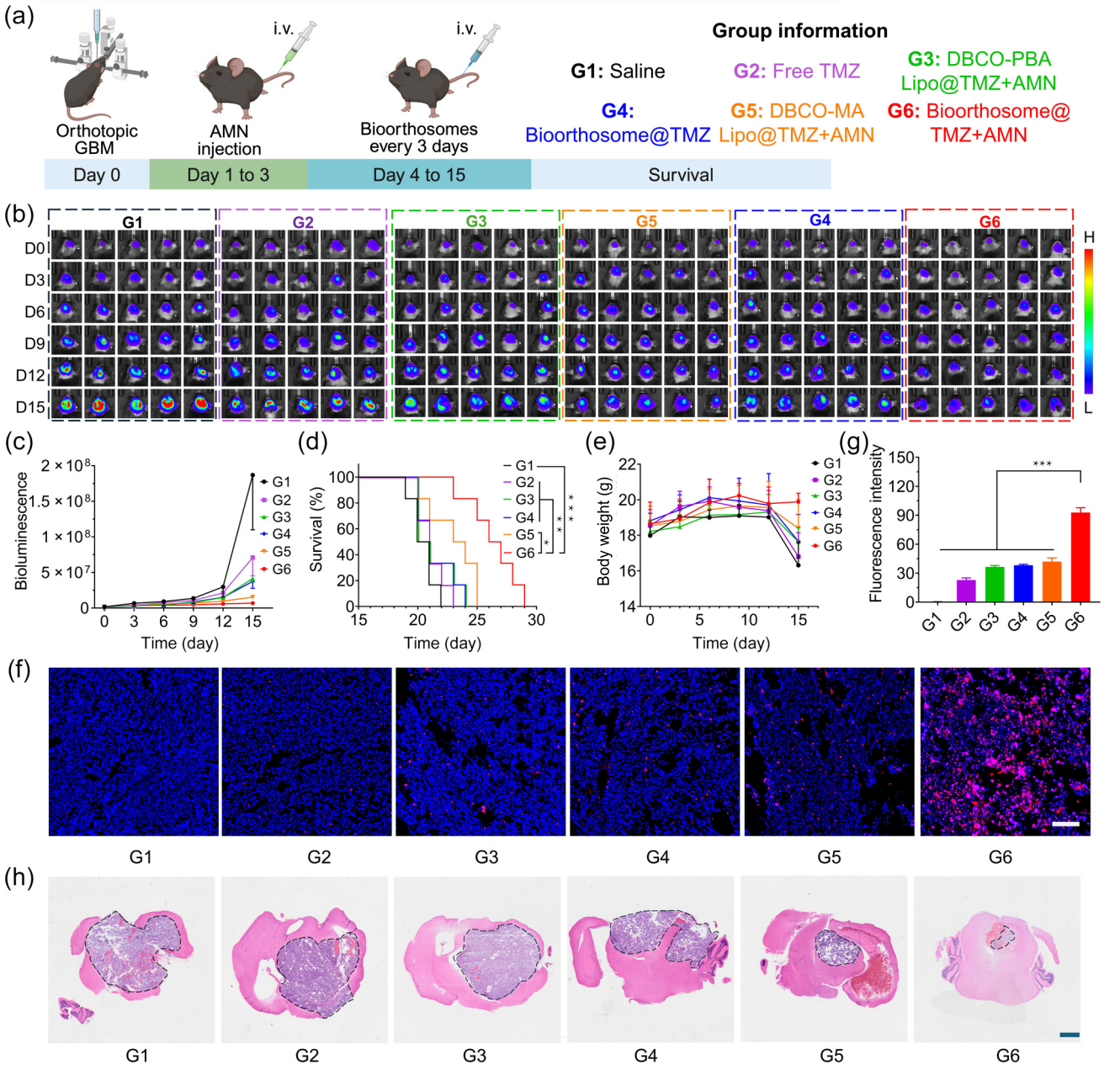

Figure 5 Enhanced liposomal delivery by Bioorthosomes in an orthotopic GBM model. (a) Diagrammatic representation of the *in vivo* experimental setup. (b) Bioluminescence imaging of intracranial GL261-Luc tumor-bearing mice across various treatment groups (n = 5). (c) Quantitative bioluminescence data revealing the progression of GBM following different therapeutic interventions (n = 5). (d) Kaplan–Meier survival plot illustrating the survival rates during the course of treatment (n = 6). (e) Monitoring of body weight fluctuations throughout the treatment period (n = 6). (f) TUNEL immunofluorescence staining of tumor sections post-treatment, with a scale bar indicating 200 μm. (g) Quantification of TUNEL-positive cells within the tumor areas after various treatments (n = 3). (h) HE stained brain sections from each treatment group, with the scale bar equals to 1 mm. The black dash enclosure indicated GBM region.

traverse the BBB and selectively target GBM through the application of switchable bioorthogonal chemistry, thereby enhancing the delivery precision of liposomal formulations to tumor cells. We specifically employed a metabolic glycoengineering strategy using AMN that could cross BBB through niacin receptor HCAR2 to *in situ* present azide-containing sialylations on the surface of GBM cells. Then we constructed the Bioorthosome by incorporating DBCO functionalities alongside a pH-activatable PBA-MA borate ester. The DBCO would facilitate the bioorthogonal reaction with azide-containing sialylations on cell surfaces, while the PBA-MA borate ester acted dualistically as a BBB-penetrating ligand through GLUT1 transporters and a shield to prevent premature bioorthogonal reactions in healthy tissue. Upon encountering the acidic TME, the MA moieties detached from the Bioorthosome, subsequently exposing the DBCO to trigger the bioorthogonal chemistry mediated GBM targeting. In comparison, the bioorthogonal chemistry would not occur in the normal brain tissue, as the DBCO was shielded. We conducted a comprehensive assessment of the targeting efficacy of the Bioorthosome both *in vitro* and *in vivo*, with the collective findings confirming the system's ability to successfully transport therapeutics across the BBB and deliver it accurately within GBM tissues, while

preventing off-target release in normal brain tissue. This distinctive feature is pivotal for augmenting therapeutic efficacy and mitigating adverse effects in the treatment of GBM.

Electronic Supplementary Material: Supplementary material (synthetic process of DSPE-PEG-PBA, DSPE-PEG-MA, and Ac_3ManNAz-NA, MALDI-TOF-MS of DSPE-PEG-PBA and DSPE-PEG-MA, ESI-MS spectrum and ^{1}H NMR of Ac_3ManNAz-NA, boronate ester bonds assay, size distribution and PDI distribution of DBCO-PBA Lipo, MTT assay of free TMZ in GL261-Luc cells, *in vivo* images, Fluorescence images of the GL261-Luc GBM-bearing brain tissues, HE staining histopathology results, and hemolytic analysis) is available in the online version of this article at https://doi.org/10.26599/NR.2025.94907338.

Data availability

All data needed to support the conclusions in the paper are presented in the manuscript and the Electronic Supplementary Material. Additional data related to this paper may be requested from the corresponding author upon request.

Acknowledgments

The authors gratefully acknowledge the support from the National Natural Science Foundation of China (Nos. 82172084, 81803002, and 32371342), STI2030-Major Projects (No. 2022ZD0212500), Shanghai Frontiers Science Center of Drug Target Identification and Delivery (No. ZXWH2170101), Shaanxi Provincial Education Department serves local industrialization projects (No. 20JC035), Xi'an Science and Technology Bureau of Shaanxi province-scientific and technological personnel service enterprise project (No. 22GXFW0133) and Shaanxi innovation team project (No. 2023-CX-TD-58). The Scheme was drawn by Biorender.com.

Declaration of competing interest

All the contributing authors report no conflict of interests in this work.

Author contribution statement

C. W.: Data curation, formal analysis, investigation, methodology, project administration, visualization, writing – original draft. J. W.: Data curation, methodology, visualization. Z. R. D.: Formal analysis. Y. Q. P.: Data curation. H. J. Q.: Methodology. W. C.: Methodology. N. W.: Methodology. H. C.: Data curation. X. L. G.: Data curation. M. Q. H.: Investigation. Y. Z.: Funding acquisition, methodology, project administration, writing – review & editing. X. D. X.: Conceptualization, funding acquisition, methodology, project administration, writing – review & editing.

Informed consent

Not applicable.

Ethics statement

The animal experiments were carried out following the guidelines of the Animal Use and Care Administrative Advisory Committee of Shanghai Jiao Tong University (Approval Number: A2024180).

Use of AI statement

None.

References

[1] Louis, D. N.; Perry, A.; Wesseling, P.; Brat, D. J.; Cree, I. A.; Figarella-Branger, D.; Hawkins, C.; Ng, H. K.; Pfister, S. M.; Reifenberger, G. et al. The 2021 WHO classification of tumors of the central nervous system: A summary. *Neuro Oncol.* **2021**, *23*, 1231–1251.

[2] Price, M.; Ballard, C.; Benedetti, J.; Neff, C.; Cioffi, G.; Waite, K. A.; Kruchko, C.; Barnholtz-Sloan, J. S.; Ostrom, Q. T. CBTRUS statistical report: Primary brain and other central nervous system tumors diagnosed in the united states in 2017-2021. *Neuro-Oncol.* **2024**, *26*, vi1–vi85.

[3] Weller, M.; Wen, P. Y.; Chang, S. M.; Dirven, L.; Lim, M.; Monje, M.; Reifenberger, G. Glioma. *Nat. Rev. Dis. Primers* **2024**, *10*, 33.

[4] Arvanitis, C. D.; Ferraro, G. B.; Jain, R. K. The blood-brain barrier and blood-tumour barrier in brain tumours and metastases. *Nat. Rev. Cancer* **2020**, *20*, 26–41.

[5] Ruan, S. B.; Zhou, Y.; Jiang, X. G.; Gao, H. L. Rethinking CRITID procedure of brain targeting drug delivery: Circulation, blood brain barrier recognition, intracellular transport, diseased cell targeting, internalization, and drug release. *Adv. Sci.* **2021**, *8*, 2004025.

[6] Xue, X. D.; Qu, H. J.; Li, Y. P. Stimuli-responsive crosslinked nanomedicine for cancer treatment. *Exploration* **2022**, *2*, 20210134.

[7] Zhang, D. Y.; Sun, Y. J.; Wang, S. Y.; Zou, Y.; Zheng, M.; Shi, B. Y. Brain-targeting metastatic tumor cell membrane cloaked biomimetic nanomedicines mediate potent chemodynamic and RNAi combinational therapy of glioblastoma. *Adv. Funct. Mater.* **2022**, *32*, 2209239.

[8] Tong, F.; Zhou, Y.; Xu, Y. Y.; Chen, Y. X.; Yudintceva, N.; Shevtsov, M.; Gao, H. L. Supramolecular nanomedicines based on host-guest interactions of cyclodextrins. *Exploration* **2023**, *3*, 20210111.

[9] Cheng, W.; Qu, H. J.; Yang, J. J.; Chen, H.; Pan, Y. Q.; Duan, Z. R.; Xue, X. D. Hierarchically engineered self-adaptive nanoplatform guided intuitive and precision interventions for deep-seated glioblastoma. *ACS Nano* **2025**, *19*, 557–579.

[10] Li, S. J.; Meng, C. T.; Hao, Q.; Zhou, R. N.; Dai, L. Y.; Guo, Y. C.; Zhao, S. T.; Zhou, X.; Lou, C. J.; Xu, J. et al. "On/off"-switchable crosslinked PTX-nanoformulation with improved precise delivery for NSCLC brain metastases and restrained adverse reaction over nab-PTX. *Biomaterials* **2024**, *307*, 122537.

[11] Anraku, Y.; Kuwahara, H.; Fukusato, Y.; Mizoguchi, A.; Ishii, T.; Nitta, K.; Matsumoto, Y.; Toh, K.; Miyata, K.; Uchida, S. et al. Glycaemic control boosts glucosylated nanocarrier crossing the BBB into the brain. *Nat. Commun.* **2017**, *8*, 1001.

[12] Zhang, Y.; Qu, H. J.; Xue, X. D. Blood-brain barrier penetrating liposomes with synergistic chemotherapy for glioblastoma treatment. *Biomater. Sci.* **2022**, *10*, 423–434.

[13] Jiang, S. P.; Li, W. P.; Yang, J.; Zhang, T.; Zhang, Y. Q.; Xu, L.; Hu, B.; Li, Z.; Gao, H. L.; Huang, Y. Y. et al. Cathepsin B-responsive programmed brain targeted delivery system for chemo-immunotherapy combination therapy of glioblastoma. *ACS Nano* **2024**, *18*, 6445–6462.

[14] Zou, Y.; Sun, X. H.; Yang, Q. S.; Zheng, M.; Shimoni, O.; Ruan, W. M.; Wang, Y. B.; Zhang, D. Y.; Yin, J. L.; Huang, X. G. et al. Blood-brain barrier-penetrating single CRISPR–Cas9 nanocapsules for effective and safe glioblastoma gene therapy. *Sci. Adv.* **2022**, *8*, eabm8011.

[15] Ruan, S. B.; Qin, L.; Xiao, W.; Hu, C.; Zhou, Y.; Wang, R. R.; Sun, X.; Yu, W. Q.; He, Q.; Gao, H. L. Acid-responsive transferrin dissociation and GLUT mediated exocytosis for increased blood-brain barrier transcytosis and programmed glioma targeting delivery. *Adv. Funct. Mater.* **2018**, *28*, 1802227.

[16] Liu, Y. J.; Wang, W. D.; Zhang, D. Y.; Sun, Y. J.; Li, F. Z.; Zheng, M.; Lovejoy, D. B.; Zou, Y.; Shi, B. Y. Brain co-delivery of first-line chemotherapy drug and epigenetic bromodomain inhibitor for multidimensional enhanced synergistic glioblastoma therapy. *Exploration* **2022**, *2*, 20210274.

[17] Liu, Y. J.; Zhang, D. Y.; An, Y.; Sun, Y. J.; Li, J.; Zheng, M.; Zou, Y.; Shi, B. Y. Non-invasive PTEN mRNA brain delivery effectively mitigates growth of orthotopic glioblastoma. *Nano Today* **2023**, *49*, 101790.

[18] Tylawsky, D. E.; Kiguchi, H.; Vaynshteyn, J.; Gerwin, J.; Shah, J.; Islam, T.; Boyer, J. A.; Boué, D. R.; Snuderl, M.; Greenblatt, M. B. et al. P-selectin-targeted nanocarriers induce active crossing of the blood-brain barrier via caveolin-1-dependent transcytosis. *Nat. Mater.* **2023**, *22*, 391–399.

[19] Pandit, R.; Chen, L. Y.; Götz, J. The blood-brain barrier: Physiology and strategies for drug delivery. *Adv. Drug Delivery Rev.* **2020**, *165–166*, 1–14.

[20] Yang, J.; Li, Y.; Jiang, S. P.; Tian, Y. X.; Zhang, M. J.; Guo, S.; Wu, P. F.; Li, J. N.; Xu, L.; Li, W. P. et al. Engineered brain-targeting exosome for reprogramming immunosuppressive microenvironment of glioblastoma. *Exploration*, in press, DOI: 10.1002/EXP.20240039.

[21] Zou, Y.; Wang, Y. B.; Xu, S.; Liu, Y. J.; Yin, J. L.; Lovejoy, D. B.; Zheng, M.; Liang, X. J.; Park, J. B.; Efremov, Y. M. et al. Brain co-delivery of temozolomide and cisplatin for combinatorial glioblastoma chemotherapy. *Adv. Mater.* **2022**, *34*, 2203958.

[22] Fan, Q.; Kuang, L.; Wang, B. Y.; Yin, Y.; Dong, Z. F.; Tian, N. X.; Wang, J. J.; Yin, T. Y.; Wang, Y. Z. Multiple synergistic effects of the microglia membrane-bionic nanoplatform on mediate tumor microenvironment remodeling to amplify glioblastoma immunotherapy. *ACS Nano* **2024**, *18*, 14469–14486.

[23] Cheng, W.; Duan, Z. R.; Chen, H.; Wang, Y. J.; Wang, C.; Pan, Y. Q.; Wu, J.; Wang, N.; Qu, H. J.; Xue, X. D. Macrophage membrane-camouflaged pure-drug nanomedicine for synergistic chemo- and interstitial photodynamic therapy against glioblastoma. *Acta Biomater.* **2025**, *193*, 392–405.

[24] Yoon, H. Y.; Koo, H.; Kim, K.; Kwon, I. C. Molecular imaging based on metabolic glycoengineering and bioorthogonal click chemistry. *Biomaterials* **2017**, *132*, 28–36.

[25] Zheng, C. X.; Wang, Q. X.; Wang, Y.; Zhao, X. Z.; Gao, K. M.; Liu, Q.; Zhao, Y.; Zhang, Z. Z.; Zheng, Y. D.; Cao, J. J. et al. *In situ* modification of the tumor cell surface with immunomodulating nanoparticles for effective suppression of tumor growth in mice. *Adv. Mater.* **2019**, *31*, e1902542.

[26] Chang, P. V.; Chen, X.; Smyrniotis, C.; Xenakis, A.; Hu, T. S.; Bertozzi, C. R.; Wu, P. Metabolic labeling of sialic acids in living animals with alkynyl sugars. *Angew. Chem., Int. Ed.* **2009**, *48*, 4030–4033.

[27] Fan, M.; Zhang, X.; Liu, H. F.; Li, L. Y.; Wang, F.; Luo, L.; Zhou, X. H.; Liang, X. J.; Zhang, J.; Li, Z. H. Reversing immune checkpoint inhibitor-associated cardiotoxicity via bioorthogonal metabolic engineering-driven extracellular vesicle redirecting. *Adv. Mater.* **2024**, *36*, 2412340.

[28] Laughlin, S. T.; Bertozzi, C. R. Metabolic labeling of glycans with azido sugars and subsequent glycan-profiling and visualization via staudinger ligation. *Nat. Protoc.* **2007**, *2*, 2930–2944.

[29] Hudak, J. E.; Canham, S. M.; Bertozzi, C. R. Glycocalyx engineering reveals a siglec-based mechanism for NK cell immunoevasion. *Nat. Chem. Biol.* **2014**, *10*, 69–75.

[30] Kelly, P. N. The cancer immunotherapy revolution. *Science* **2018**, *359*, 1344–1345.

[31] Lu, X. Y.; Xu, Z. X.; Shu, F.; Wang, Y. D.; Han, Y. H.; Yang, X. R.; Shi, P. L.; Fan, C. Q.; Wang, L. L.; Yu, F. et al. Reactive oxygen species responsive multifunctional fusion extracellular nanovesicles: Prospective treatments for acute heart transplant rejection. *Adv. Mater.* **2024**, *36*, 2406758.

[32] Koo, H.; Lee, S.; Na, J. H.; Kim, S. H.; Hahn, S. K.; Choi, K.; Kwon, I. C.; Jeong, S. Y.; Kim, K. Bioorthogonal copper-free click chemistry *in vivo* for tumor-targeted delivery of nanoparticles. *Angew. Chem., Int. Ed.* **2012**, *51*, 11836–11840.

[33] Yang, J. J.; Yang, K. Y.; Du, S. Y.; Luo, W.; Wang, C.; Liu, H. M.; Liu, K. G.; Zhang, Z. B.; Gao, Y. F.; Han, X. et al. Bioorthogonal reaction-mediated tumor-selective delivery of CRISPR/Cas9 system for dual-targeted cancer immunotherapy. *Angew. Chem.* **2023**, *135*, e202306863.

[34] Shajahan, A.; Parashar, S.; Goswami, S.; Ahmed, S. M.; Nagarajan, P.; Sampathkumar, S. G. Carbohydrate-neuroactive hybrid strategy for metabolic glycan engineering of the central nervous system *in vivo*. *J. Am. Chem. Soc.* **2017**, *139*, 693–700.

[35] Wu, H.; Lu, H. W.; Xiao, W. W.; Yang, J. F.; Du, H. X.; Shen, Y. B.; Qu, H. J.; Jia, B.; Manna, S. K.; Ramachandran, M. et al. Sequential targeting in crosslinking nanotheranostics for tackling the multibarriers of brain tumors. *Adv. Mater.* **2020**, *32*, 1903759.

[36] Saxon, E.; Bertozzi, C. R. Cell surface engineering by a modified staudinger reaction. *Science* **2000**, *287*, 2007–2010.

[37] Charter, N. W.; Mahal, L. K.; Koshland, D. E. Jr. ; Bertozzi, C. R. Differential effects of unnatural sialic acids on the polysialylation of the neural cell adhesion molecule and neuronal behavior. *J. Biol. Chem.* **2002**, *277*, 9255–9261.

[38] Li, T. L.; Xu, D.; Ruan, Z.; Zhou, J.; Sun, W. B.; Rao, B.; Xu, H. B. Metabolism/immunity dual-regulation thermogels potentiating immunotherapy of glioblastoma through lactate-excretion inhibition and PD–1/PD–L1 blockade. *Adv. Sci.* **2024**, *11*, e2310163.

[39] Wang, X. L.; Ding, B. B.; Liu, W.; Qi, L. S.; Li, J. T.; Zheng, X.; Song, Y. Q.; Li, Q. Y.; Wu, J. W.; Zhang, M. et al. Dual starvations induce pyroptosis for orthotopic pancreatic cancer therapy through simultaneous deprivation of glucose and glutamine. *J. Am. Chem. Soc.* **2024**, *146*, 17854–17865.